Surface Reflectance from Commercial Very High Resolution Multispectral Imagery Estimated Empirically with Synthetic Landsat (2023)

Paul M. Montesano, Matthew J. Macander, Jordan A. Caraballo-Vega, Melanie J. Frost, Christopher S. R. Neigh, Gerald V. Frost, Glenn S. Tamkin, and Mark L. Carroll

***Abstract*— Scientific analysis of Earth's land surface change benefits from well-characterized multispectral remotely sensed data for which models estimate and remove the effects of the atmosphere and sun-sensor geometry. Top-of-atmosphere (TOA) reflectance in commercial very high resolution (< 5 m; VHR) spaceborne imagery routinely varies for unchanged surfaces because of signal variation from these effects. To reliably identify critical broad-scale environmental change, consistency from surface reflectance (SR) versions of this imagery must be sufficient to identify and track the change or stability of fine-scale features that, though small, may be widely distributed across remote and heterogeneous domains. Commercial SR products are available, but typically the model employed is proprietary and their use is prohibitively costly for large spatial extents. Here we (1) describe and apply an open-source workflow for the scientific community for fine-scaled empirical estimation of surface reflectance from multispectral VHR imagery using reference from synthetic Landsat surface reflectance, (2) examine SR model results and compare with corresponding TOA estimates for a large batch with varying acquisitions in Arctic and Sub-Arctic regions, (3) assess its consistency at pseudo-invariant calibration sites, and (4) quantify improvements in classification of land cover in a Sahelian region. Results show this workflow is best for longer wavelength optical bands, identifies poor estimates associated with image acquisition variation using context provided from large batches of VHR, improves estimates with robust regression models, produces consistent estimates for non-varying sites through time, and can increase the accuracy of land cover assessments.**

***Index Terms*—Remote Sensing, Surface Reflectance, Very High Resolution**

I. INTRODUCTION

NASA Earth Observing System missions produce properly calibrated, science quality remotely sensed datasets [1]. This data quality is the result of models that estimate and remove atmospheric constituents and account for acquisition characteristics [2], [3], [4]. The use of these data for a wide range of science and applications has become widely accepted [5] because the satellite data are well calibrated, documented, understood, and accessible [6], [7], [8], [9], [10].

The provision of spaceborne remote sensing data is evolving as commercial providers serve an increasing role in earth observation [11], [12], [13], [14], [15]. These providers collect spaceborne imagery at very high spatial resolution (< 5 m; VHR). As VHR archives increase, time-series of these data can be used for additional scientific purposes beyond calibration and validation [15] that include quantifying changes in glacier mass balance [16], forest structure [17], [18], and land cover [14], and monitoring biodiversity [19] and human conflict [20]. However, to do this, scene-to-scene VHR image consistency in radiometric fidelity requires a conversion from top-of-atmosphere reflectance to surface reflectance (SR) [21], due to the routine signal variation of unchanged surface features from the combined effects of atmospheric constituents, aerosols, and a range of sun-sensor geometric scenarios of acquisitions [22], [23]. Consistency from this imagery must be sufficient to identify and track the change or stability of fine-scale features that, though small, may be widely distributed across remote domains, and serve as key indicators of critical broad-scale environmental variation and change [11], [24].

Several atmospheric correction methods and algorithms have been developed for a variety of multispectral imagery. Two types of these algorithms include those that are (1) image-based empirical corrections (e.g., the empirical line method [25], dark-object subtraction [26], Quick Atmospheric Correction [27]) and (2) physically-based corrections (e.g., the Fast Line of Sight Atmospheric Analysis of Spectral Hypercubes (FLAASH) [28], the Framework for Operational Radiometric Correction for Environmental monitoring (FORCE) [29], the Landsat Surface Reflectance Code (LaSRC) [30], the multi-angle implementation of atmospheric correction for MODIS (MAIAC) [8], and the Simplified and Robust Surface Reflectance Estimation Method (SREM) [31]).

Image-based corrections work within single image datasets without needing external reference and are efficient but lack a common frame of reference for reflectance. Physically-based corrections for commercial multispectral VHR (e.g., Maxar Worldview-1/2/3), while rigorous, are difficult to implement for several reasons. First, these data often lack the necessary atmospheric correction bands. Specifically, only Worldview-3 has 12 cloud, aerosol, vapor, ice, and snow (CAVIS) bands (30 m) that can be used to provide spatially explicit atmospheric parameters used for correction. Second, the fine resolution imposes unique anisotropic effects that, for regions with vegetation, depend in part on its vertical and horizontal structure [32], [33] that may not be sufficiently characterized. Third, existing atmospheric corrections algorithms rely on parameterization that is not optimized for fully automated workflows often required for processing large volumes of

VHR data [33], [34]. Furthermore, previous calibration and SR estimation that relate Maxar data to near coincident MODIS surface reflectance data [8], [15], [35] rely on coarse resolution reference (1 km). While commercial SR products are available, they typically employ a model that is proprietary and the costs for using these products across large batches of VHR imagery over large geographic domains can be significant (e.g., Planet Surface Reflectance v.2 [36] and Maxar's AComp [37]). As such, an open-source SR estimation approach that overcomes the challenges imposed by the need for reference across multiple adjacent VHR images, the lack of physically-based correction requirements, and commercial proprietary restrictions may be useful to the scientific community working with VHR imagery over heterogenous land covers spanning broad spatial extents.

Here, we present a workflow to estimate SR for spaceborne VHR imagery using corresponding synthetic Landsat surface reflectance data and apply it to sets of VHR imagery across a variety of landscapes to assess its performance for fine-scaled estimation of surface reflectance. We examine the correspondence of SR estimates to source TOA for a large batch with varying acquisitions, assess its consistency at calibration sites, and quantify accuracy gains in land cover classification.

II. Study Areas

In this study we apply a surface reflectance estimation workflow (Fig. 1) on three different regions and extents to examine and evaluate surface reflectance estimates from VHR across a range of conditions. The first region is a broad spatial extent over Alaska (Fig. 2) associated with boreal forest and tundra land covers. The second region is White Sands, New Mexico, USA (Fig. 4), a frequently used area for image calibration due to the pseudo-invariant nature of its land surface. The third features mosaics of smallholder agriculture and natural Sahelian land covers in Senegal (Fig. 6). These study areas include primarily natural or human-modified vegetation landscapes with little human infrastructure, and therefore our methods and analyses are not designed for land covers with predominately urban and built features.

III. Methodology

Fig. 1 summarizes the workflow to estimate SR from input VHR. This workflow is designed to improve the consistency of VHR imagery within large commercial data archives that are available to the US Government [38], in particular QuickBird-2, GeoEye-1, Worldview-1/2/3/4, and enable analysis of fine-scaled phenomena across broad spatial extents and through time. It highlights the two data inputs required for the estimation of SR from VHR, that of the source VHR itself and the reference SR estimates from synthetic Landsat [39].

(Figure 1 at end)

Fig. 1. The workflow for estimating surface reflectance for commercial VHR multispectral imagery (SR_{VHR}).

The VHR surface reflectance workflow compiles an input data stack that combines (1) existing procedures that prepare input VHR with (2) surface reflectance reference ($SR_{reference}$) from synthetic Landsat for SR estimation from VHR imagery (SR_{VHR}), and (3) builds and applies the SR_{VHR} model. First, $SR_{reference}$ from synthetic Landsat is compiled for VHR imagery. Next, "enhanced" VHR data (eVHR) are produced by processing level 1B (seamless, geometrically- and radiometrically-corrected mosaics of sub-images [40]) imagery to orthorectified top-of-atmosphere reflectance (TOA_{VHR}) [15], [41] and then applying an automated cloud-masking [42] procedure before using them as input to a procedure to model surface reflectance. This SR procedure stacks all input layers into a common modeling grid (e.g., 30 m; coarser than the input TOA) grid for the input TOA spatial extent, derives a mask from invalid data in each of the 3 input datasets, applies that mask to the input TOA and reference SR to remove all invalid pixels, builds an SR model at 30 m resolution, and applies that model to the original VHR TOA at 2 m spatial resolution.

A. Preparing input synthetic Landsat reference and VHR imagery

We compiled $SR_{reference}$ for temporally and spatially coincident VHR imagery using an algorithm to synthesize Landsat-derived SR [39] based on the archive of Landsat data. The model parameters used to create synthetic $SR_{reference}$ are generated from the record of all available Landsat 4/5/7/8/9 Tier 1 Level 2 surface reflectance observations that are masked to exclude cloud, cloud shadows, snow, pixels that are saturated in any band, and gaps. Then, we use the projection, bounding box and acquisition date of the input VHR image to generate a synthetic (modeled) map of estimated SR based on the harmonic model parameters of the Landsat time-series. These model parameters describe variations in surface reflectance derived from seasonality, inter-annual trends, and disturbances that appear within the Landsat surface reflectance record from 1984-2020 [43].

Next, we computed TOA_{VHR} reflectance using the workflow described in Neigh et al. 2019 [15]. This returned an orthorectified multispectral stack in cloud-optimized geotiff format that is georeferenced to the local Universal Transverse Mercator coordinate system in a grid with a resolution native to the input TOA_{VHR} (2 m). To identify valid surface pixels, we applied a convolutional neural net algorithm to mask cloud cover for each TOA_{VHR} [42]. The mask is returned as a binary map that separates cloud from non-cloud pixels. In some cases, transparent cirrus clouds are not identified as such, while some very bright non-cloud surfaces (smooth snow cover or bright lichen ground cover extents) may be mis-classified as clouds. Therefore, the development of this algorithm continues as new training data is acquired. These steps resulted in a set of three input datasets ($SR_{reference}$, input TOA_{VHR}, and cloud cover mask of input TOA_{VHR}) for the re-gridding and masking steps, prior to model building.

The input files were re-gridded by reprojecting each to the coordinate system of the input TOA_{VHR} and coarsening to the 30 m pixel resolution of the reference. These re-gridding steps

use the mean for the reflectance bands and mode for the cloud mask. Re-gridding the 2 m inputs to the coarser spatial resolution of the 30 m $SR_{reference}$ at this stage makes for efficient model building. After re-gridding, we build a common mask that includes all "no data" collected from both $SR_{reference}$ and input TOA_{VHR} datasets. This mask is thus a union of all input "no data", however, because we use synthetic Landsat which provides valid reference values for all pixels of an extent, the "no data" extent for this study represents the just the masked cloudcover pixels from the input TOA. Both $SR_{reference}$ and input TOA_{VHR} are masked with this common mask so that the same set of pixels are present in each dataset. At this point, each input TOA_{VHR} pixel has a corresponding reference pixel, and the data is ready for model building.

B. Building and applying the surface reflectance correction: the SR_{VHR} workflow

We use the re-gridded and masked data stack to build a linear model using ordinary least squares (OLS) regression to describe the relationship of the input TOA_{VHR} (dependent) to the $SR_{reference}$ (independent). The models are applied to bandwise pairs for the blue, green, red, and near-infrared bands (Band 7, or NIR1, in the case of Worldview-2/3/4), where a given TOA_{VHR} band is paired with the closest corresponding $SR_{reference}$ band based on the central wavelength. The bandwise model fit that is returned based on the model choice (OLS) is then applied back to corresponding input TOA_{VHR} band (2 m). This is done for each band of the input TOA_{VHR} to return the multi-band surface reflectance estimates at 2 m spatial resolution (SR_{VHR}).

We applied this workflow in a distributed manner on NASA Goddard Space Flight Center's computational platform Explore to a sample of hundreds of VHR image strips at sites in Alaska, New Mexico, and Senegal. This large sample provided opportunities to examine and evaluate the performance of the workflow where (1) acquisition sun-sensor geometry can vary significantly (Alaska), (2) where surface reflectance variation is effectively absent (pseudo-invariant calibration site near White Sands, New Mexico, USA), and where on-going studies require VHR reflectance precision through time to distinguish subtle patterns of land-use change (Senegal). These sites span a range of environmental conditions, disturbance histories, physiographic regions, and land covers across boreal, tundra, desert, and Sahel landscapes.

C. Assessing estimates of surface reflectance from VHR

We assessed estimates of SR_{VHR} in three ways. First, using VHR in Alaska, we examined the correspondence of SR_{VHR} estimates to TOA_{VHR} and $SR_{reference}$ for a large batch for which there was important variation in sun-sensor geometry of acquisitions. To do this, we randomly sampled 0.1% of the 2 m pixels to build a database of corresponding input TOA_{VHR}, $SR_{reference}$, and output SR_{VHR} estimates. Next, to examine the consistency at pseudo-invariant calibration sites we compared SR_{VHR} and TOA_{VHR} pixels at 50 randomly selected sites for which we acquired a decadal-scale time series of VHR. Finally, to quantify accuracy gains in land cover classification, we compared the accuracy of tree, crop, and other vegetation classifications derived from SR_{VHR} and TOA_{VHR} across landscapes dominated by anthropogenic land-use and land cover changes in the Sahel region of Senegal.

The land cover classes were derived from a UNet-based convolutional neural network classification model [44] applied to both SR_{VHR} and TOA_{VHR}. Training data was built through a combination of semi-supervised and manual iterations for label enhancement [45] and divided using a 70/30 split into training and test sets. An additional set of independent validation points were produced following land cover evaluation best practices [46]. Three different observers were assigned to each scene using a collaborative tool designed for earth observation validation [47], which enabled the rapid generation of randomly stratified observations to be validated by each observer.

Independent models were trained for both SR_{VHR} and TOA_{VHR}, where input and label tiles come from the same exact locations, with the only difference being the SR_{VHR} and TOA_{VHR} input values. These models were then trained until convergence using the cross-entropy loss function and the Adam optimizer, with early stopping monitoring based on the minimization of the loss function [45]. Geometric data augmentation was performed during model training to increase the dataset size, while retaining the spectral information of the training tiles [42]. Inference was performed using the best output from each model to produce end-to-end land cover maps using the *tensorflow-caney* software framework [44], [48].

IV. Results

The results we present and discuss below were produced with an open-source containerized version of the SR_{VHR} workflow [49] designed and evaluated for routine use across large volumes of VHR data on high performance compute platforms. Our results are derived from the application of this workflow across hundreds of individual Maxar images. Results are divided into three subsections on the variation of VHR imagery, assessing the consistency of SR_{VHR} through time, and quantifying the improvements in land cover classification from SR_{VHR}.

A. Assessing variation to optimize VHR image selection

The first set of results highlights the variation of VHR imagery, where bandwise relationships between image types provide a performance evaluation for assessing which images benefit most from this empirical SR estimation. Results from a batch (n=170) of VHR imagery in Alaska (Fig. 2a) draws on comparisons between SR_{VHR}, TOA_{VHR}, and $SR_{reference}$ in Arctic and Sub-Arctic regions. There are three key results from these comparisons:

- SR_{VHR} vs TOA_{VHR} comparisons vary across multi-spectral bands,
- SR_{VHR} model results can vary significantly according to input VHR sun elevation angles, and
- SR_{VHR} model estimation choice can optimize SR_{VHR} estimation.

The results of these comparisons guide the selection of specific VHR images from within a large archive in which variation in

acquisition characteristics can affect image consistency across a broad spatial extent. Fig. 2b,c,d, highlights the variation in band performance. The slopes from linear models of TOA_{VHR} versus $SR_{reference}$ (Fig. 2b) along with their SR_{VHR} counterparts (Fig. 2c) show bands corresponding to longer wavelengths result in better correspondence with reference reflectance due to lower atmospheric scattering. The SR_{VHR} yield the strongest relationships bandwise with $SR_{reference}$, where the relationships of the blue bands improve from $R^2 = 0.29$ (TOA_{VHR}) to $R^2 = 0.57$ (SR_{VHR}). Overall, the NIR bands from SR_{VHR} show the highest level of agreement with $SR_{reference}$ ($R^2 = 0.83$).

The skyplot in Fig. 2a and the plots in Fig. 2d,e highlight the potential sensitivity of SR_{VHR} results to solar elevation angle. This sensitivity is important because it provides a means to identify outlier VHR acquisitions within large groups for an area of interest. Fig. 2a features a cluster of frequent acquisition solar geometries in the southern portion of the skyplot, as well as outlier solar geometries in the northwestern section associated with summer evening acquisitions during low light conditions in the high northern latitudes. These outlier solar elevation angles from VHR acquisitions (<15°) feature linear model slopes from the comparison of SR_{VHR} to TOA_{VHR} that are significantly less than 1 (< 0.6), providing a quantitative flag of VHR acquisitions associated with poor SR models that contribute to the scatter observed in Figure 2b,c.

(Figure 2 at end)

Fig. 2. (a) Surface reflectance was estimated for a set of 170 VHR images across Alaska with a range of acquisition solar (orange dots) and sensor view positions (black dots) summarized in the inset skyplot below the map. This range helps explain the variation shown in the evaluation of SR_{VHR} results (b-e).

Fig. 3 indicates the potential to optimize the normalization of SR estimates from VHR images across a broad and heterogenous extent using robust regression model choices other than ordinary least squares (OLS). Results show the distributions of model slopes grouped by regression model choice across each multispectral VHR band form the set of Alaska imagery. Here, the distribution of model slopes across each band feature median slope values closer to 1 for longer wavelength bands. Similarly, median slope values are closer to 1 for the robust regression model choices from reduced major axis (RMA) and Huber relative to OLS. These robust regression model choices account for error in the dependent variable and are less sensitive to outliers than OLS, respectively. They offer an improvement in the adjustment of pixels across a broader range of reflectance values over the OLS method, which is important for calibrating surface reflectance for bright and dark targets such as lichen understories, bright bare surfaces and soils, and inundated herbaceous vegetation.

(Figure 3 at end)

Fig. 3. The regression model choice can optimize the normalization of surface reflectance estimates. Boxplots summarize the distribution of model slopes across the set of VHR images for 3 linear model options. Robust regression model choices using RMA and Huber result in model slopes closer to 1 than OLS. These robust regression model choices improve the adjustment of pixels across a broader range of reflectance values over that from ordinary least squares regression, which is important for calibrating bright and dark targets.

B. Consistency in surface reflectance time-series at a pseudo-invariant site

We quantified the consistency of estimates from TOA_{VHR} and SR_{VHR} versions of multispectral acquisitions at a pseudo-invariant site. These sites experience little change through time and are assumed to have consistent surface reflectance. Fig. 4 shows a map of 50 randomly distributed locations for which multiple acquisitions span a decadal-scale time series of multispectral TOA_{VHR} and corresponding SR_{VHR} within a pseudo-invariant site area near White Sands, NM. Using one of the 50 points as an example, the plot tracks reflectance values for each multispectral band of each image type across a time-series of 6 June-September VHR images (QuickBird-2 and Worldview-2) from 2002-2013. Fig. 5 shows the distributions of the band-wise slopes calculated from a time-series at each of the 50 locations within a 12.63- year time span at the pseudo-invariant analysis site. Together, these time-series results confirm that the SR_{VHR} estimates maintain the expected consistency of reflectance estimates through time at a site of no significant change, where distribution of time-series slopes even indicate a marginal improvement in consistency in SR_{VHR} over TOA_{VHR} across all bands.

(Figure 4 at end)

Fig. 4. Decadal-scale time-series of VHR observations explains the stability of the derived SR_{VHR} from the source TOA_{VHR} reflectance. Here, overlapping extents of VHR imagery produce a dense time-series of observations within the analysis extent of this pseudo-invariant calibration area near White Sands, New Mexico, USA. A set of 50 randomly sampled time-series analysis sites were collected and mapped in this analysis extent to form a consistent calibration sample. The plot (right) shows an example from a single analysis site of a time-series of SR_{VHR} and TOA_{VHR} reflectance across 11 years (2002-2013) with 6 seasonal (June-September) VHR images from both QuickBird-2 (QB02) and Worldview-2 (WV02).

(Figure 5 at end)

Fig. 5. The distributions of the slopes of each of the 50 analysis site time-series across the full (12.63 year) time span at the calibration site in White Sands, New Mexico, USA. While both SR_{VHR} and TOA_{VHR} slope distributions yield median values near 0, indicative of no change in reflectance at the site, the SR_{VHR} distributions return a marginally more accurate no-change estimate than do the corresponding TOA_{VHR} estimates across each of the multispectral bands.

C. Quantifying land cover classification improvements

The consistency presented above in SR_{VHR} is particularly valuable when data are used for land cover assessments. We quantified improvements in land cover classification from SR_{VHR} relative to their TOA_{VHR} counterparts. To do this, we report classifications of 3 land cover types at a variety of study sites distributed across 3 biogeographic regions (Senegal River Valley, Casamance, Eastern Transition Zone) in Senegal. We summarize these classification improvements using 2-4 classification accuracy statistics (*user accuracy*, *producer accuracy*, *recall*, *precision*, and *accuracy*) from each set of input to the reference validation set for individual classes of 'crop', 'tree', and 'other' (non-tree or crop vegetation) and a combined class ('overall') [42]. Generally, accuracy gains were achieved using the SR_{VHR} in place of the corresponding TOA_{VHR} as input into the classification model both overall and across the 3 individual classes 'crop', 'tree', and 'other'. Here, improvement from SR_{VHR} is demonstrated with generally higher median classification accuracy values and smaller ranges of accuracy statistic distributions.

(Figure 6 at end)

Fig. 6. Classification accuracy rates across classification sites in three Sahelian regions in Senegal. This comparison of accuracy rates for land cover classes from SR_{VHR} show smaller distributions than TOA_{VHR} imagery.

V. Discussion

The concept of 'science-ready' or 'analysis-ready' VHR spaceborne data refers to imagery that has undergone formatting and calibration in preparation for rigorous geospatial analysis. This study presents a workflow that performs cloud-optimized formatting and an empirical surface reflectance estimation, and evaluates image outputs from this SR modeling workflow for application across large volumes of VHR imagery.

The SR modeling that we present and evaluate represents a simple and straightforward method for estimating surface reflectance. It does not involve image-specific parameterization that is part of physically-based atmospheric compensation models. As such, this method is not as rigorous as existing methods (e.g., MAIAC, FLAASH), where specific atmospheric components are accounted for individually. In fact, it is more similar to image-based methods that use look-up table approaches to evaluate surface reflectance. However, the 'look-up table' approach that we use here is location-specific yet features a consistency across continuous spatial extents. In this work, for any given 30 m location, we "look-up" (predict) a pixel's expected bandwise surface reflectance by leveraging the per-pixel history of reflectance captured in the Landsat record that is available for all land surfaces. The existing (pre-built) calculation of the harmonic patterns, linear trends, and identification of breakpoints within this record [39] provides the basis for prediction of $SR_{reference}$. Furthermore, it enables on-demand prediction of per-pixel $SR_{reference}$ given what is expected based on the intra- and inter-annual patterns captured for a given location within the Landsat record. This allows for precise (daily) matching of $SR_{reference}$ with TOA_{VHR} at 30 m resolution and is a key component to our SR estimation.

Noteworthy is the source of the $SR_{reference}$ and its potential effect on the SR_{VHR} results. The synthetic $SR_{reference}$ are based on 30 m data and are thus likely more appropriate for reflectance standardization in land covers where biophysically relevant variation occurs at patch scales (~ 10 m^2 – 100 m^2), often across rapid seasonality gradients. However, Landsat-derived reference will be less robust in routinely cloudy regions, particularly when cloudiness is unevenly distributed through seasonal cycles. Furthermore, because we use the Landsat record up through 2020, VHR data post-2020 may feature changes (e.g., disturbance from fires) that are not accounted for in the Landsat record we used to create our reference.

This simpler approach is designed to be used across hundreds to thousands of VHR images. Primarily, it provides a means for efficient standardization of VHR images. This step is critical a-priori step before detailed vegetation structure and land cover analyses, where optimizing the across-image standardization is important for a few reasons. First, it can improve the consistency of image mosaics needed for robust analyses of regional extents at meter-scales. Second, it can improve the consistency of a time-series, reducing the differences in reflectance among non-changing features. Finally, the use of synthetic Landsat SR as reference leverages a globally available reflectance history catalog for which, when used to standardize VHR, may enable powerful cross-scale time-series analyses and detailed biophysical modeling opportunities. A meta-analysis to compare our SR_{VHR} results to those from other methods was not performed as part of this study but would be an important to quantify the spatial uncertainties of this SR method and clarify key trade-offs.

VI. Conclusions

We assembled a workflow to estimate surface reflectance for 2 m resolution multispectral VHR imagery based on synthetic reference derived from the full Landsat record. We applied this workflow to hundreds of VHR images across a wide range of geographic domains and time periods and examined the variation of SR image results within large batches across multi-spectral bands, acquisition characteristics, and SR model estimation choices. We assessed the consistency of SR results across a time-series, and the accuracy of classified land cover. Results show that this SR workflow is best for longer wavelength optical bands, identifies poor estimates associated with VHR image acquisition variation using context provided from large batches of VHR, improves estimates with robust regression models, produces consistent estimates for non-varying sites through time, and can increase the accuracy of land cover assessments. This workflow, and its open-source container deployment, extends the accessibility and utility of spaceborne VHR data for scientists, because it is designed to improve standardization within large batches of imagery. It provides a means to routinely prepare otherwise difficult-to-handle datasets for analysis of land cover and vegetation structure patterns across space and time at sub-decameter spatial scales and is particularly useful for work in areas of high environmental heterogeneity that are experiencing subtle yet significant changes.

REFERENCES

[1] E. Chuvieco and C. Justice, "NASA Earth Observation Satellite Missions for Global Change Research," in *Earth Observation of Global Change*, E. Chuvieco, Ed., Dordrecht: Springer Netherlands, 2008, pp. 23–47. doi: 10.1007/978-1-4020-6358-9_2.

[2] G. Doxani *et al.*, "Atmospheric Correction Inter-Comparison Exercise," *Remote Sensing*, vol. 10, no. 2, p. 352, Feb. 2018, doi: 10.3390/rs10020352.

[3] E. Vermote, C. Justice, M. Claverie, and B. Franch, "Preliminary analysis of the performance of the Landsat 8/OLI land surface reflectance product," *Remote Sensing of Environment*, vol. 185, pp. 46–56, Nov. 2016, doi: 10.1016/j.rse.2016.04.008.

[4] R. Richter and D. Schläpfer, "Geo-atmospheric processing of airborne imaging spectrometry data. Part 2: Atmospheric/topographic correction," *International Journal of Remote Sensing*, vol. 23, no. 13, pp. 2631–2649, Jan. 2002, doi: 10.1080/01431160110115834.

[5] N. Earth Science Data Systems, "Earth Science Data and Information System (ESDIS) Project | Earthdata." Accessed: Aug. 20, 2024. [Online]. Available: https://www.earthdata.nasa.gov/esdis

[6] M. Feng, C. Huang, S. Channan, E. F. Vermote, J. G. Masek, and J. R. Townshend, "Quality assessment of Landsat surface reflectance products using MODIS data," *Computers & Geosciences*, vol. 38, no. 1, pp. 9–22, Jan. 2012, doi: 10.1016/j.cageo.2011.04.011.

[7] M. Feng *et al.*, "Global surface reflectance products from Landsat: Assessment using coincident MODIS observations," *Remote Sensing of Environment*, vol. 134, pp. 276–293, Jul. 2013, doi: 10.1016/j.rse.2013.02.031.

[8] A. I. Lyapustin *et al.*, "Multi-angle implementation of atmospheric correction for MODIS (MAIAC): 3. Atmospheric correction," *Remote Sensing of Environment*, vol. 127, pp. 385–393, Dec. 2012, doi: 10.1016/j.rse.2012.09.002.

[9] J. G. Masek *et al.*, "A Landsat Surface Reflectance Dataset for North America, 1990–2000," *IEEE Geosci. Remote Sensing Lett.*, vol. 3, no. 1, pp. 68–72, Jan. 2006, doi: 10.1109/LGRS.2005.857030.

[10] "Common Metadata Repository (CMR) | Earthdata." Accessed: Aug. 20, 2024. [Online]. Available: https://www.earthdata.nasa.gov/eosdis/science-system-description/eosdis-components/cmr

[11] P. M. Montesano, G. Sun, R. O. Dubayah, and K. J. Ranson, "Spaceborne potential for examining taiga–tundra ecotone form andvulnerability," *Biogeosciences*, vol. 13, no. 13, pp. 3847–3861, Jul. 2016, doi: 10.5194/bg-13-3847-2016.

[12] M. Brandt *et al.*, "Reduction of tree cover in West African woodlands and promotion in semi-arid farmlands," *Nature Geosci*, vol. 11, no. 5, pp. 328–333, May 2018, doi: 10.1038/s41561-018-0092-x.

[13] S. W. Cooley, L. C. Smith, J. C. Ryan, L. H. Pitcher, and T. M. Pavelsky, "Arctic-Boreal Lake Dynamics Revealed Using CubeSat Imagery," *Geophysical Research Letters*, vol. 46, no. 4, pp. 2111–2120, Feb. 2019, doi: 10.1029/2018GL081584.

[14] C. S. R. Neigh *et al.*, "Smallholder crop area mapped with wall-to-wall WorldView sub-meter panchromatic image texture: A test case for Tigray, Ethiopia," *Remote Sensing of Environment*, vol. 212, pp. 8–20, Jun. 2018, doi: 10.1016/j.rse.2018.04.025.

[15] C. S. R. Neigh *et al.*, "An API for Spaceborne Sub-Meter Resolution Products for Earth Science," in *IGARSS 2019 - 2019 IEEE International Geoscience and Remote Sensing Symposium*, Yokohama, Japan: IEEE, Jul. 2019, pp. 5397–5400. doi: 10.1109/IGARSS.2019.8898358.

[16] D. E. Shean, S. Bhushan, P. Montesano, D. R. Rounce, A. Arendt, and B. Osmanoglu, "A Systematic, Regional Assessment of High Mountain Asia Glacier Mass Balance," *Front. Earth Sci.*, vol. 7, p. 363, Jan. 2020, doi: 10.3389/feart.2019.00363.

[17] J. Wang, D. Liu, S. M. Quiring, and R. Qin, "Estimating canopy height change using machine learning by coupling WorldView-2 stereo imagery with Landsat-7 data," *International Journal of Remote Sensing*, vol. 44, no. 2, pp. 631–645, Jan. 2023, doi: 10.1080/01431161.2023.2169596.

[18] P. M. Montesano, C. S. R. Neigh, W. Wagner, M. Wooten, and B. D. Cook, "Boreal canopy surfaces from spaceborne stereogrammetry," *Remote Sensing of Environment*, vol. 225, pp. 148–159, May 2019, doi: 10.1016/j.rse.2019.02.012.

[19] A. K. Skidmore, "Priority list of biodiversity metrics to observe from space".

[20] M. M. Bennett, J. Van Den Hoek, B. Zhao, and A. V. Prishchepov, "Improving Satellite Monitoring of Armed Conflicts," *Earth's Future*, vol. 10, no. 9, p. e2022EF002904, 2022, doi: 10.1029/2022EF002904.

[21] M. Nazeer *et al.*, "Evaluation of atmospheric correction methods for low to high resolutions satellite remote sensing data," *Atmospheric Research*, vol. 249, p. 105308, Feb. 2021, doi: 10.1016/j.atmosres.2020.105308.

[22] R. Richter, "Correction of atmospheric and topographic effects for high spatial resolution satellite imagery," *International Journal of Remote Sensing*, vol. 18, no. 5, pp. 1099–1111, Mar. 1997, doi: 10.1080/014311697218593.

[23] P. S. Chavez, "Image-Based Atmospheric Corrections - Revisited and Improved," 1996.

[24] M. K. Ward Jones, W. H. Pollard, and B. M. Jones, "Rapid initialization of retrogressive thaw slumps in the Canadian high Arctic and their response to climate and terrain factors," *Environ. Res. Lett.*, vol. 14, no. 5, p. 055006, May 2019, doi: 10.1088/1748-9326/ab12fd.

[25] E. Karpouzli and T. Malthus, "The empirical line method for the atmospheric correction of IKONOS imagery," *International Journal of Remote Sensing*, vol. 24, no. 5, pp. 1143–1150, Jan. 2003, doi: 10.1080/0143116021000026779.

[26] P. S. Chavez, "An improved dark-object subtraction technique for atmospheric scattering correction of multispectral data," *Remote Sensing of Environment*, vol. 24, no. 3, pp. 459–479, Apr. 1988, doi: 10.1016/0034-4257(88)90019-3.

[27] L. S. Bernstein, "Quick atmospheric correction code: algorithm description and recent upgrades," *Opt. Eng*,

vol. 51, no. 11, p. 111719, Jul. 2012, doi: 10.1117/1.OE.51.11.111719.

[28] G. P. Anderson *et al.*, "MODTRAN4-based atmospheric correction algorithm: FLAASH (fast line-of-sight atmospheric analysis of spectral hypercubes)," in *Algorithms and Technologies for Multispectral, Hyperspectral, and Ultraspectral Imagery VIII*, SPIE, Aug. 2002, pp. 65–71. doi: 10.1117/12.478737.

[29] D. Frantz, "FORCE—Landsat + Sentinel-2 Analysis Ready Data and Beyond," *Remote Sensing*, vol. 11, no. 9, Art. no. 9, Jan. 2019, doi: 10.3390/rs11091124.

[30] E. Vermote, C. Justice, M. Claverie, and B. Franch, "Preliminary analysis of the performance of the Landsat 8/OLI land surface reflectance product," *Remote Sensing of Environment*, vol. 185, pp. 46–56, Nov. 2016, doi: 10.1016/j.rse.2016.04.008.

[31] M. Bilal *et al.*, "A Simplified and Robust Surface Reflectance Estimation Method (SREM) for Use over Diverse Land Surfaces Using Multi-Sensor Data," *Remote Sensing*, vol. 11, no. 11, Art. no. 11, Jan. 2019, doi: 10.3390/rs11111344.

[32] P. M. Montesano, C. Neigh, G. Sun, L. Duncanson, J. Van Den Hoek, and K. J. Ranson, "The use of sun elevation angle for stereogrammetric boreal forest height in open canopies," *Remote Sensing of Environment*, vol. 196, pp. 76–88, Jul. 2017, doi: 10.1016/j.rse.2017.04.024.

[33] J. L. Pancorbo, B. T. Lamb, M. Quemada, W. D. Hively, I. Gonzalez-Fernandez, and I. Molina, "Sentinel-2 and WorldView-3 atmospheric correction and signal normalization based on ground-truth spectroradiometric measurements," *ISPRS Journal of Photogrammetry and Remote Sensing*, vol. 173, pp. 166–180, Mar. 2021, doi: 10.1016/j.isprsjprs.2021.01.009.

[34] G. P. Anderson *et al.*, "MODTRAN4-based atmospheric correction algorithm: FLAASH (fast line-of-sight atmospheric analysis of spectral hypercubes)," presented at the AeroSense 2002, S. S. Shen and P. E. Lewis, Eds., Orlando, FL, Aug. 2002, pp. 65–71. doi: 10.1117/12.478737.

[35] M. Choi *et al.*, "Calibration of Maxar Constellation Over Libya-4 Site Using MAIAC Technique," *IEEE J. Sel. Top. Appl. Earth Observations Remote Sensing*, vol. 17, pp. 5460–5469, 2024, doi: 10.1109/JSTARS.2024.3367250.

[36] Collison, A., and N. Wilson, "Planet Surface Reflectance Product.," in *Technical White Paper: Version1*, 2017, pp. 671–672.

[37] F. Pacifici, N. Longbotham, and W. J. Emery, "The Importance of Physical Quantities for the Analysis of Multitemporal and Multiangular Optical Very High Spatial Resolution Images," *IEEE Trans. Geosci. Remote Sensing*, vol. 52, no. 10, pp. 6241–6256, Oct. 2014, doi: 10.1109/TGRS.2013.2295819.

[38] C. S. R. Neigh, J. G. Masek, and J. E. Nickeson, "High-Resolution Satellite Data Open for Government Research," *EoS Transactions*, vol. 94, no. 13, pp. 121–123, Mar. 2013, doi: 10.1002/2013EO130002.

[39] Z. Zhu, C. E. Woodcock, C. Holden, and Z. Yang, "Generating synthetic Landsat images based on all available Landsat data: Predicting Landsat surface reflectance at any given time," *Remote Sensing of Environment*, vol. 162, pp. 67–83, Jun. 2015, doi: 10.1016/j.rse.2015.02.009.

[40] D. E. Shean *et al.*, "An automated, open-source pipeline for mass production of digital elevation models (DEMs) from very-high-resolution commercial stereo satellite imagery," *ISPRS Journal of Photogrammetry and Remote Sensing*, vol. 116, pp. 101–117, Jun. 2016, doi: 10.1016/j.isprsjprs.2016.03.012.

[41] Caleb Spradlin, Savannah Strong Finch, and mwooten3, *nasa-nccs-hpda/evhr: release/2.2.0*. (Nov. 01, 2023). Zenodo. doi: 10.5281/ZENODO.10062471.

[42] J. A. Caraballo-Vega *et al.*, "Optimizing WorldView-2, -3 cloud masking using machine learning approaches," *Remote Sensing of Environment*, vol. 284, p. 113332, Jan. 2023, doi: 10.1016/j.rse.2022.113332.

[43] Z. Zhu and C. E. Woodcock, "Continuous change detection and classification of land cover using all available Landsat data," *Remote Sensing of Environment*, vol. 144, pp. 152–171, Mar. 2014, doi: 10.1016/j.rse.2014.01.011.

[44] J. A. Caraballo-Vega and C. Spradlin, *nasa-nccs-hpda/tensorflow-caney: 0.4.2*. (Feb. 12, 2024). Zenodo. doi: 10.5281/zenodo.10652004.

[45] M. T. Le *et al.*, "Training Strategies of Cnn for Land Cover Mapping with High Resolution Multi-Spectral Imagery in Senegal," in *IGARSS 2023 - 2023 IEEE International Geoscience and Remote Sensing Symposium*, Pasadena, CA, USA: IEEE, Jul. 2023, pp. 6358–6361. doi: 10.1109/IGARSS52108.2023.10283308.

[46] P. Olofsson, G. M. Foody, M. Herold, S. V. Stehman, C. E. Woodcock, and M. A. Wulder, "Good practices for estimating area and assessing accuracy of land change," *Remote Sensing of Environment*, vol. 148, pp. 42–57, May 2014, doi: 10.1016/j.rse.2014.02.015.

[47] J. A. Caraballo-Vega, *nasa-nccs-hpda/eo-validation: 0.0.2*. (Sep. 28, 2023). Zenodo. doi: 10.5281/ZENODO.8386759.

[48] J. A. Caraballo-Vega *et al.*, "Remote Sensing Powered Containers for Big Data and AI/ML Analysis: Accelerating Science, Standardizing Operations," in *IGARSS 2022 - 2022 IEEE International Geoscience and Remote Sensing Symposium*, Kuala Lumpur, Malaysia: IEEE, Jul. 2022, pp. 4034–4037. doi: 10.1109/IGARSS46834.2022.9883436.

[49] gtamkin, *nasa-nccs-hpda/srlite: srlite_2.0.0-20240315-baseline*. (Aug. 07, 2024). Zenodo. doi: 10.5281/ZENODO.13256144.

1459

Figure 1

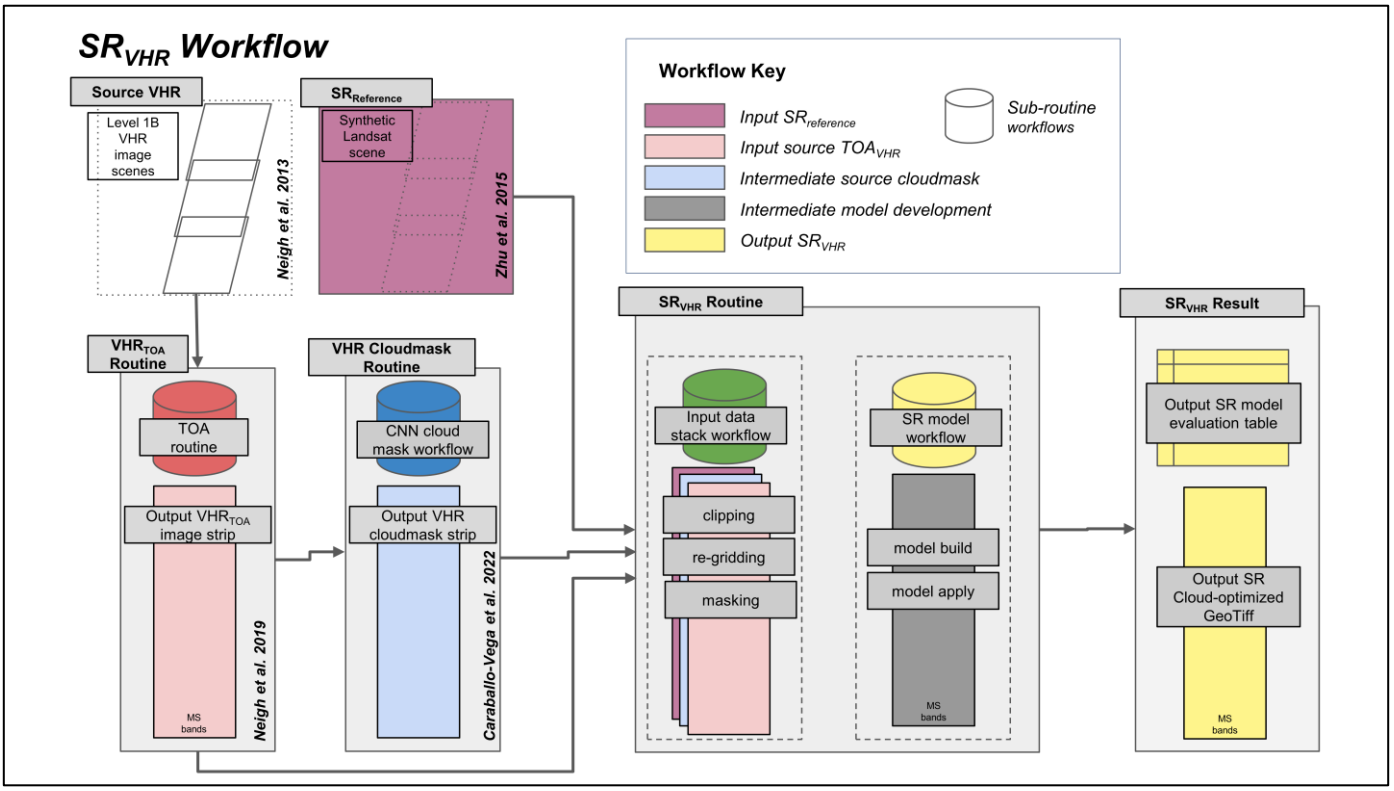

Figure 2

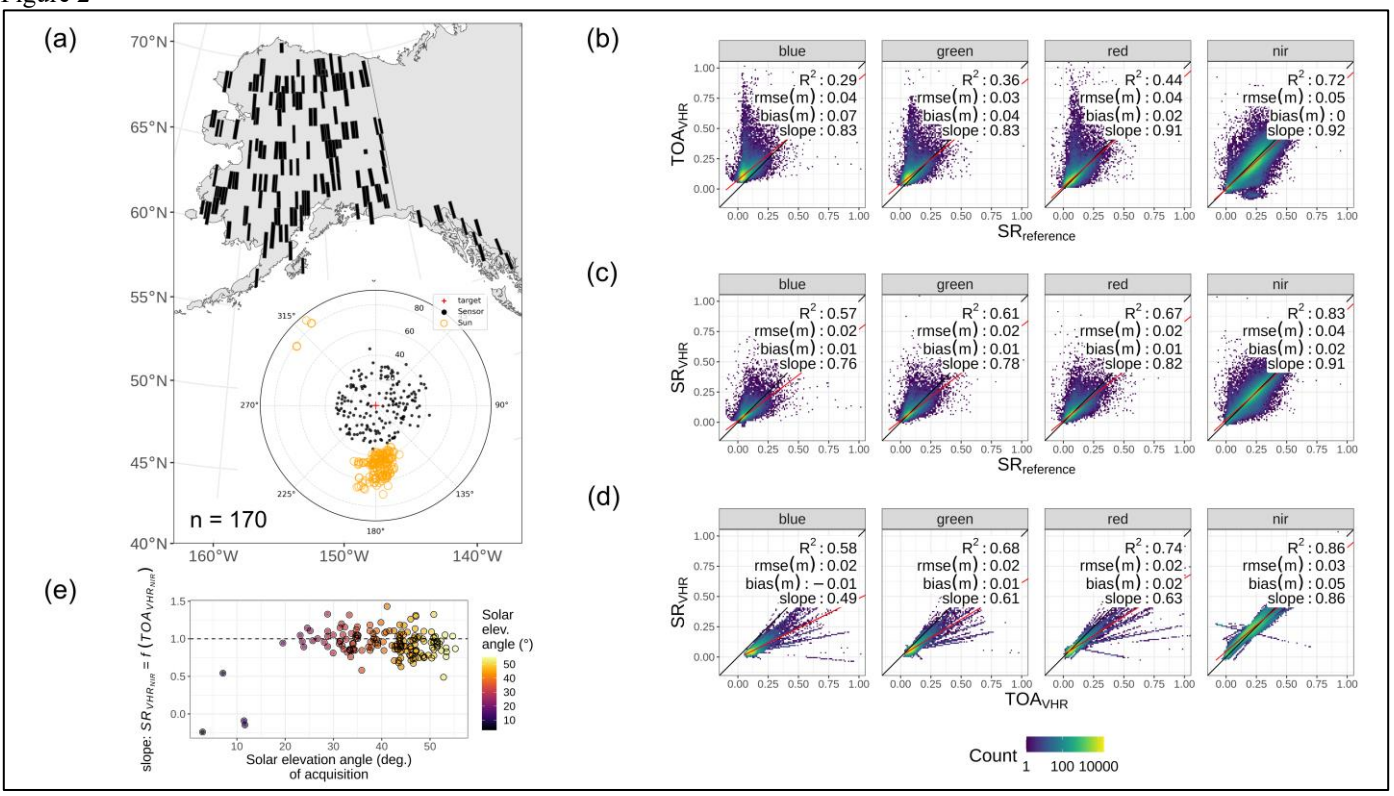

Figure 3

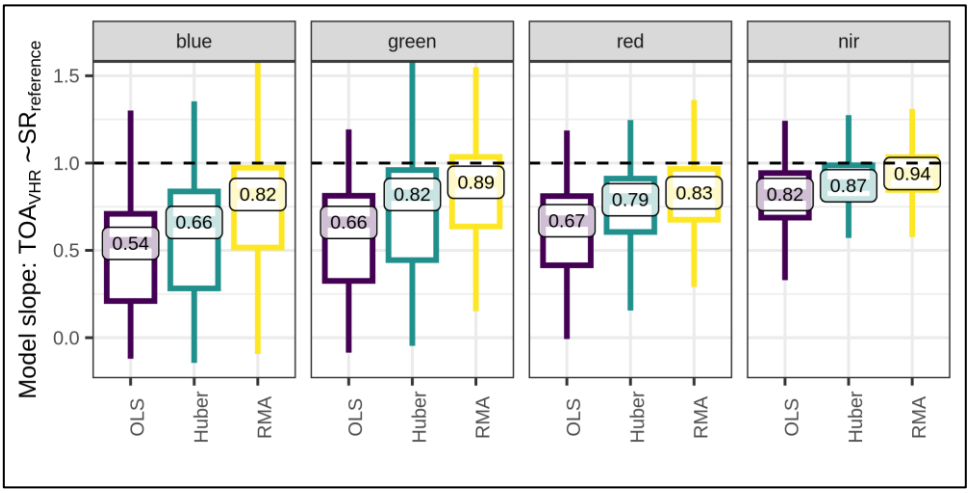

Figure 4

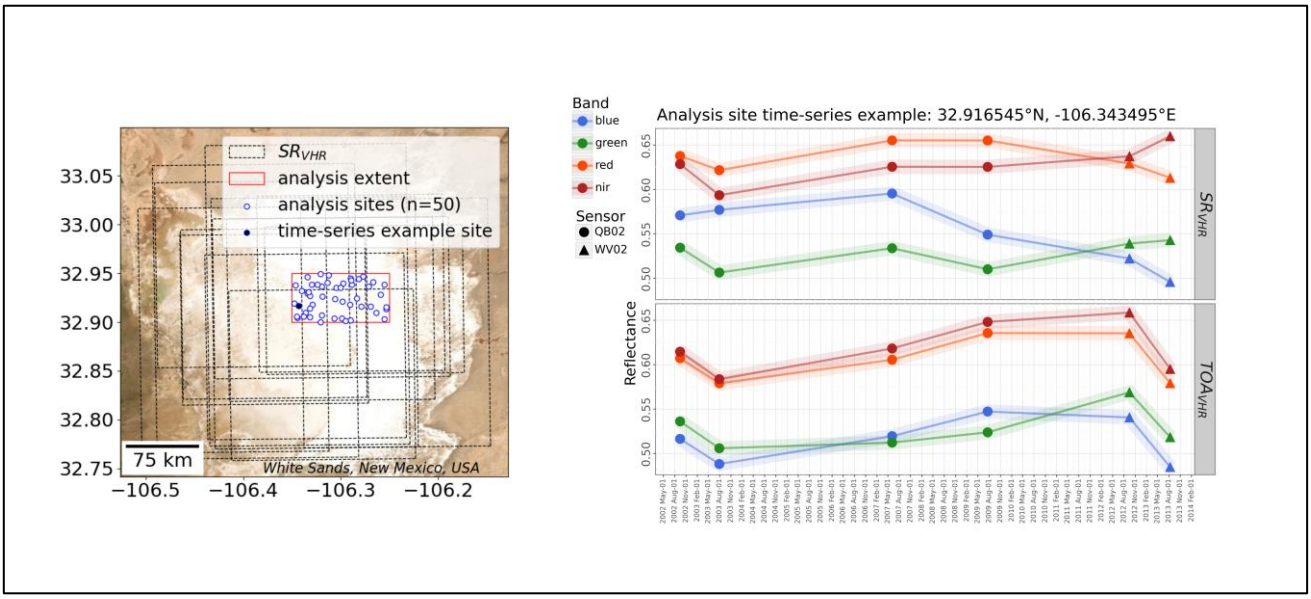

Figure 5

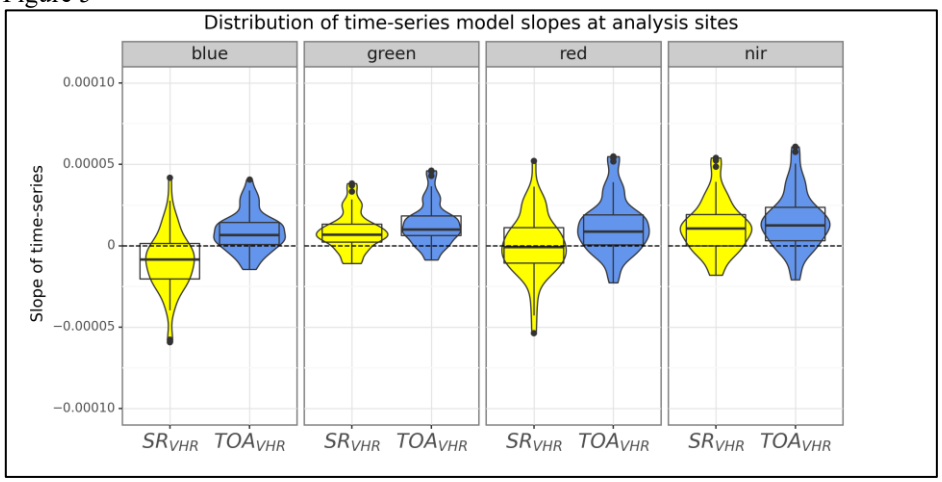

Figure 6